

# Investigating the influence of the calendering process on the 3D microstructure of single-layer and two-layer cathodes in lithium-ion batteries using synchrotron tomography

Marten Ademmer<sup>a,\*</sup>, Benedikt Priffing<sup>a</sup>, Manuel Weller<sup>b</sup>, André Hilger<sup>c</sup>, Markus Osenberg<sup>c</sup>, Ingo Manke<sup>c</sup>, Volker Knoblauch<sup>d</sup>, Volker Schmidt<sup>a</sup>

<sup>a</sup>*Institute of Stochastics, Ulm University, 89069 Ulm, Germany*

<sup>b</sup>*VARTA Microbattery GmbH, 73479 Ellwangen, Germany*

<sup>c</sup>*Institute of Applied Materials, Helmholtz-Zentrum Berlin für Materialien und Energie GmbH, 14109 Berlin, Germany*

<sup>d</sup>*Materials Research Institute, Aalen University, 73430 Aalen, Germany*

---

## Abstract

Lithium-ion batteries are one of the most important devices for the storage of electrical energy. Further improvement of their performance is a central goal in state-of-the-art battery research to satisfy the permanently growing demands. It is well known that this can be achieved by optimizing the 3D microstructure of the electrodes, which in turn depends on the material composition used as well as on the corresponding production parameters. Since the calendering process of electrodes has a significant impact on their microstructure, the goal of this paper is to further deepen the understanding of how varying the compaction load changes the microstructure of lithium-ion battery cathodes. For this purpose, three different sample sets are analyzed and compared to each other, using image data gained by synchrotron tomography. More precisely, we consider differently compacted thin and thick cathodes as well as a set of porosity-graded two-layer cathode samples. A phase-based as well as a particle-based segmentation of the tomographic image data is performed to allow for an extensive morphological analysis of the cathode samples, where, among others, mean geodesic tortuosity and constrictivity of the pore space as well as particle connectivity are considered to quantify changes of the 3D microstructure. Furthermore, for the two-layer sample set, a special focus is put on microstructural changes of both layers and the interface between them.

*Keywords:* Cathode, lithium-ion battery, microstructure, two-layer electrode, synchrotron tomography, statistical image analysis

---

## 1. Introduction

Lithium-ion batteries are used in a broad range of applications like mobile phones, laptops and electric vehicles because of their high power and energy density as well as low discharge rate [1, 2, 3, 4].

---

\*Corresponding author. Email: marten.ademmer@uni-ulm.de. Phone: +49 731 50 - 23555. Fax: +49 731 50 - 23649.

Increasing electrification of the transport system and the transformation of the fossil fuel dependent electrical grid to a system that relies on renewable energies lead to a steadily growing demand for Li-ion batteries with optimized effective properties [5, 6]. Therefore, it is important to improve their electrochemical performance with regard to, for example, the energy density and cycling stability [4]. Optimizing the morphology of anodes and cathodes is a promising approach to achieve this goal since a major factor influencing the performance of a battery is their 3D microstructure [7, 8, 9, 10, 11, 12, 13, 14]. For this purpose, 3D image data obtained by X-ray tomography is frequently used [15, 16, 17, 18, 19]. Moreover, the 3D microstructure of such electrodes depends significantly on the underlying materials as well as the production process [20], where the latter, among others, consists of mixing [21, 22], drying [23, 24] and calendaring [25, 26]. Thus, it is crucial to understand how different production parameters influence the resulting morphology of an electrode.

The aforementioned calendaring step during the production process is of great importance, as it heavily influences the density of the electrode and thereby significantly alters the transport paths within the composite electrode [18]. In general, higher compaction loads lead to higher energy densities and an increased active material connectivity, which in turn means a loss of connectivity in the pore space and, thereby, can strongly limit transport within the electrolyte. This reflects the general trade-off between high energy and high power cells [1]. Therefore, it is important to have a detailed understanding of how different compaction loads influence the 3D microstructure of battery electrodes. For example, the 3D microstructure of cathodes manufactured with an arbitrary compaction load is predicted in [27], using a parametric stochastic 3D microstructure model based on methods from stochastic geometry [28, 29]. Beyond calendaring, a further direct approach to increase the energy density is given by increasing the thickness of the electrode [30, 31, 32, 33]. However, this hinders charge transport due to longer transport paths [30, 34, 35, 36, 37, 38]. One promising approach to overcome these limitations are two-layer electrodes [39, 40, 41], where a different porosity in each layer aims to combine the high energy density of the strongly compacted layer with a sufficiently connected pore space within the other layer [42, 43, 44, 45, 46]. Thus, the present paper investigates the 3D microstructure of four two-layer cathodes, which differ from each other in the porosity of the top layer. In addition, the results are compared to the thin single-layer cathodes analyzed in [18] as well as nine significantly thicker single-layer cathodes with the same material composition.

The rest of this paper is organized as follows. In Section 2 we describe the manufacturing process of the electrode samples, including four two-layer cathodes, as well as the tomographic imaging method. The subsequent image processing approach is discussed in Section 3, which finally leads to a phase-based as well as a particle-based segmentation. Then, in Section 4, we describe phase-based and particle-based descriptors of 3D microstructures, which are used to quantify the morphological changes within the electrodes. This is done in Section 5, where we compare the 3D microstructures of a series of eight differently compacted thin cathodes with those of nine thick cathodes, which have also been manufactured by varying the compaction load. Furthermore, a detailed morphological characterization of four two-layer cathodes is carried out, which allows us to compare single-layer electrodes with two-layer electrodes in a quantitative manner. Finally, in Section 6, the paper is concluded by a summary of the achieved results and an outlook to possible future research.

## 2. Experimental

This section describes the material composition and production process of the cathodes investigated in this paper and continues with a description of the imaging method that enables us to perform a quantitative analysis of the electrode morphology.

### 2.1. Cathode materials and sample preparation

We consider three sample sets of cathodes, denoted by A, B and C, respectively. The first sample set is given by eight differently compacted thin cathodes, which will be denoted by  $A_1, \dots, A_8$ . Note that larger indices correspond to a higher degree of compaction, i.e.,  $A_1$  corresponds to the uncompacted sample, while  $A_8$  denotes the cathode manufactured with the highest compaction load. A detailed description of the manufacturing process of these electrodes is presented in [47], whereas the quantitative influence of the compaction load on their 3D microstructure has been investigated in [18]. In general, all three sample sets share the following material composition: 92 wt% of  $\text{LiNi}_{1/3}\text{Co}_{1/3}\text{Mn}_{1/3}\text{O}_2$  as active material, carbon black (2 wt%) as well as graphite (2 wt%) as conductive additives and polyvinylidene flouride (4 wt%) as binder. The coated and dried uncompacted electrode from this production process, which will be referred to as single coated cathode, is used as starting point for the manufacturing of the thick and two-layer electrodes, which will be described in the following.

The second sample set consists of nine thick cathodes. They are denoted by  $B_1, \dots, B_9$ , analogous to sample set A, i.e., the degree of calendaring increases from  $B_1$  to  $B_9$ . To manufacture the thick electrodes, the single coated cathodes are coated a second time with the same wet film thickness. Thus, they could also be referred to as double coated. The coating process is thus simply repeated on the single coated cathode, followed by a second, identical drying process. The densification of the cathode electrodes to the appropriate densification levels takes place with a laboratory calender (MTI Corporation, MSK-HRP-MR100B). Circular cathode samples are then cut from these electrode sheets using a die cutter (MTI Corporation, Compact Precision Disc Cutter MSK-T-07).

The third sample set is composed of four two-layer cathodes denoted by  $C_1, \dots, C_4$ . In each case, the first layer (i. e. the layer contacting the current collector), which is also called bottom layer, is 56  $\mu\text{m}$  thick, whereas the thickness of the second layer (also called top layer) is 84  $\mu\text{m}$  ( $C_1$ ), 73  $\mu\text{m}$  ( $C_2$ ), 65  $\mu\text{m}$  ( $C_3$ ) and 60  $\mu\text{m}$  ( $C_4$ ), respectively. For the production of the two-layer cathodes, the single coated cathodes are calendared to the target compaction of the bottom layer. This is followed by another coating process to produce the top layer on the compacted bottom layer. Next, the two-layer electrodes are dried again. The compaction of the top layer to the appropriate compaction levels (grading of porosity), is again carried out with the laboratory calender. The circular cathode rods samples are then cut from these electrode sheets using the die cutter.

With regard to all samples described above, the electrode density is determined by measuring the thickness of each sample, using a micrometer caliper (Mitutoyo), and dividing it by its respective weight. The volume fraction of the different solid materials are then computed using the known material composition and is used later during the image segmentation process.

## 2.2. Tomographic imaging

The samples described in Section 2.1 have been measured by synchrotron tomography at the X-ray facility BAMline (BESSY II, Berlin, Germany) [48], which allows for non-destructive, high-resolution 3D images of the electrode microstructure. The synchrotron beam was generated with a wavelength shifter and monochromatized with a double multilayer monochromator to an energy of 30 keV (two-layer electrodes) and 25 keV (thick cathodes), respectively. After transmitting the sample, the monochromatic X-rays were converted into visible light with a  $\text{CdWO}_4$  scintillator. The optical set-up provided a 10 times magnification and the image was detected with a CCD camera PCO4000 with  $4008 \times 2672$  pixels. A  $1.7 \times 1.2 \text{ mm}^2$  field of view was captured with a pixel size of 438 nm. For each tomography, 2200 radiograms over an angular range of  $180^\circ$  were captured with an exposure time of 2 s. The reconstruction was calculated using “gridrec” [49], an implementation of the filtered back projection algorithm.

## 3. Processing of image data

The statistical analysis of the image data described in Section 2.2 is based on different microstructure descriptors that can be split into two groups, namely phase-based and particle-based descriptors. For this purpose, the image data is segmented into the following three phases: 1) Active material, 2) pores, and 3) the phase consisting of binder and conductive additives, which will be called binder-additive phase in the following. In addition, a particle-based segmentation is performed, which allows us to distinguish individual active particles from each other. First of all, the raw grayscale images have to be aligned and some samples need to be rotated and straightened. The proper alignment is carried out by creating a binary mask and computing the shift between the centroids of each slice of that mask. The shift-vectors created in this way are smoothed by the built-in Matlab function “smoothdata” with the robust local regression method [50]. Finally, the slices are shifted in such a way that the smoothed centroids are aligned, where trilinear interpolation is used to properly handle non-integer shifting values [51, 52]. To straighten the samples, an approach based on polynomial regression is used as described in [53]. From this point on, the 3D image data is orientated such that the current collector foil is parallel to the  $x$ - $y$ -plane of the coordinate system. The so called through-plane direction along the  $z$ -axis starts at the “separator side” and ends at the current collector, or vice versa. Note that the separator is not part of the samples and thus not visible in the tomographic image data. The through-plane direction is of particular importance since it is the main direction of ionic and electrical transport.

### 3.1. Phase-based segmentation

In order to compute the phase-based descriptors without edge effects, the image data is cropped to a reasonably sized cuboid and segmented into active material phase, pore space and binder-additive phase. Since there is no discernible contrast between pore space and binder-additive phase due to the similar linear attenuation coefficients of air and the carbon-based binder-additive phase, first the active material phase is separated from the phase consisting of binder, conductive additives and pores (in the following called the bap-phase) by applying a global threshold  $\lambda > 0$  [51, 54]. The value of  $\lambda$  is chosen such that the volume fraction of active material computed by means of 3D

image data matches the one determined from the material composition and the density of the cathodes. Finally, minor binarization artifacts are removed by eliminating unreasonably small clusters of active material as well as bap-phase using the Hoshen-Kopelman clustering algorithm [55]. Note that this post-processing step has no significant influence on the volume fractions of active material and bap-phase. Furthermore, this step will facilitate the particle-based segmentation performed later on.

From the binarized image data, the thickness of the cathode samples is computed by means of the rolling-ball approach [56], which is based on a morphological closing using a sphere as structuring element [57, 58, 59]. This allows us to compare the experimentally measured thickness to the microstructure thickness computed from the 3D image data. As can be seen in Table 1, in general there is a high agreement between the results obtained from experiment and image data. Furthermore, the slight underestimation of the measured thickness might be caused by the sample preparation, which might lead to a further minor compaction of the electrodes.

sample number	1	2	3	4	5	6	7	8	9
<b>sample set A</b>									
experimental / $\mu\text{m}$	80	61	57	54	52	51	50	49	
image data / $\mu\text{m}$	72	60	56	52	52	50	49	47	
<b>sample set B</b>									
experimental / $\mu\text{m}$	183	151	116	107	99	97	95	93	91
image data / $\mu\text{m}$	171	144	119	105	99	95	92	89	88
<b>sample set C</b>									
experimental / $\mu\text{m}$	140	129	121	116					
image data / $\mu\text{m}$	129	121	114	110					

Table 1: Thickness of cathode samples computed from the respective image data, together with the corresponding thickness obtained by experimental measurements.

In the next step, the observation window is split into ten cutouts, each with (in-plane) length and width of 500 voxels. In through-plane direction the whole thickness of the observation window is kept, since, as mentioned before, this is the main direction of ionic and electrical transport in the cathodes. Figure 1 shows 3D renderings of such cutouts for a selected cathode of each sample set and two different compaction loads. The remaining image processing steps and the computation of microstructure descriptors are carried out using those cutouts to keep the computational costs low.

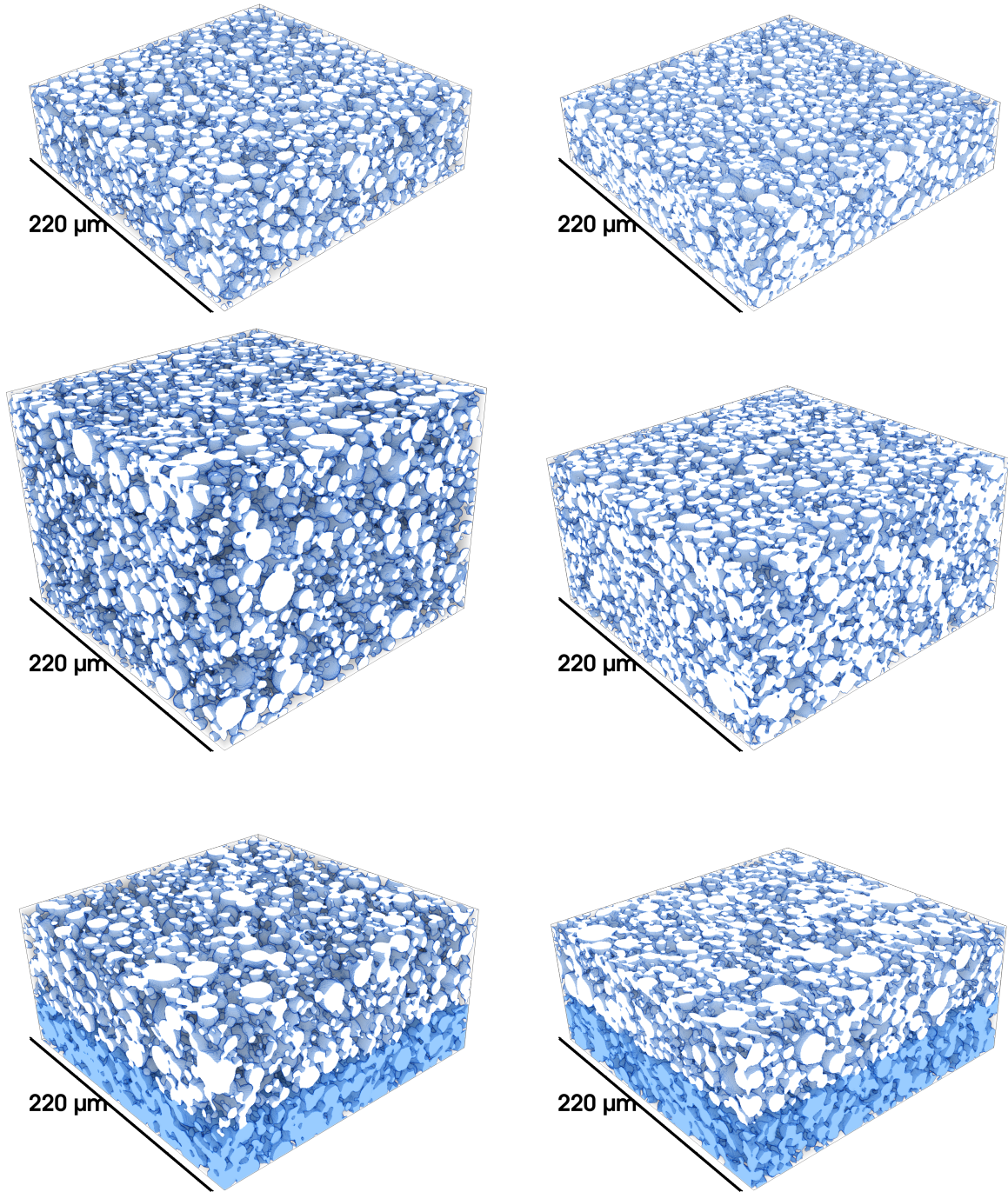


Figure 1: 3D cutout of the uncompact sample of the thin sample set ( $A_1$ , top left) and thick sample set ( $B_1$ , center left) as well as of the least compacted sample of the two layer sample set ( $C_1$ , bottom left) with highlighted second layer. The right column (sample  $A_3$ ,  $B_3$  and  $C_4$  from top to bottom) contains cathodes from the same sample set, which are manufactured with higher compaction loads.

To accurately characterize the 3D microstructure of the cathodes, the bap-phase is subdivided into pore space and binder-additive material. For this purpose, the approach considered in [18] is used. More precisely, the binder-additive phase is added by performing a morphological closing of the active material, using a ball with radius  $r > 0$  as structuring element [57, 58, 59]. For this purpose, the target volume fraction of the binder-additive phase is computed from the material composition and the density of the electrodes. Next, the bisection method is applied to determine an appropriate value of  $r$  [60]. In general, this target volume fraction can not be matched perfectly due to the discretization of image data. Thus, at first, the radius  $r$  is chosen such that the resulting volume fraction of the binder-additive phase is slightly too large. In a further step, single voxels of the added material phase are selected at random and turned back to pore space, until the expected volume fraction is reached. Note that inserting the binder-additive phase by a morphological closing of the active material leads to a reasonable spatial distribution as demonstrated in [61]. A visualization of the trinarized image data together with the underlying grayscale image is shown in Figure 2.

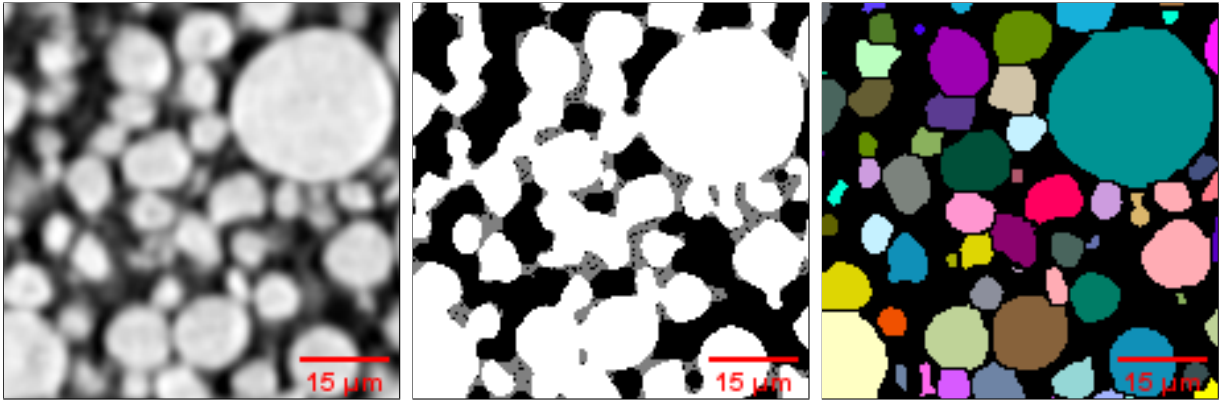


Figure 2: 2D cutout ( $66 \mu\text{m} \times 66 \mu\text{m}$ ) of the grayscale image of the uncompact thick cathode (left). The corresponding trinarization is shown in the middle, where active material, binder-additive phase and pores are depicted in white, gray and black, respectively. On the right-hand side, the segmented active particles are shown, where different colors are used for different active particles.

### 3.2. Particle-based segmentation

Last but not least, the individual active particles are extracted to enable a particle-based analysis of the 3D microstructure. A well-established method for segmenting image data of nearly spherical particles, like in the present case, is the watershed algorithm. The standard watershed algorithm floods the negative Euclidean distance transform of a binary image, starting at the local minima. So-called watershed lines are added at the locations where two different flood basins connect [62, 63]. Even though, ideally, each of those basins represents one particle, the original watershed algorithm is prone to oversegmentation. To overcome this limitation, a method based on extended regional minima is used, which depends on a single parameter  $\varepsilon_{WS} > 0$  [64]. In addition, the post-processing step considered in [65] is carried out, which involves the dilation radius  $r_{WS} > 0$ . The combination of those two approaches has turned out to be capable of successfully segmenting active material particles of cathodes in lithium-ion batteries [18, 53, 19] and is also applicable to the present data, see the plot on the right-hand side of Figure 2. The values chosen for the parameters  $\varepsilon_{WS}$  and  $r_{WS}$

sample number	1	2	3	4	5	6	7	8	9
<b>sample set A</b>									
$\varepsilon_{WS}$	1.3	1.2	1.2	1	1	0.8	0.8	0.5	
$r_{WS}$	8	7	7	7	7	6	6	6	
<b>sample set B</b>									
$\varepsilon_{WS}$	2	1.8	1.5	1.8	1.5	1.5	1.5	1.5	1.5
$r_{WS}$	5	6	6	6	6	6	6	6	6
<b>sample set C</b>									
$\varepsilon_{WS}$	1.5	1.5	1.5	1.5					
$r_{WS}$	6	6	6	6					

Table 2: Watershed parameters  $\varepsilon_{WS}$  and  $r_{WS}$  used for the sample sets A, B and C, where the values of both parameters are given in voxels.

can be found in Table 2. Note that the active particle system of the two-layer cathodes can be segmented with the same values of  $\varepsilon_{WS}$  and  $r_{WS}$  since they share the more densified layer at the current collector.

#### 4. Microstructure descriptors

In this section various microstructure descriptors are introduced, which allow us to quantitatively analyze the 3D morphology of the cathode samples. In particular, we consider phase-based descriptors, which are computed based on the trinarized image data. Furthermore, several particle-based descriptors are computed for the segmented active particles, which have been determined by the modified watershed algorithm described in Section 3.

##### 4.1. Phase-based descriptors

We first recall the meaning of several phase-based descriptors, which are used later on to quantitatively analyze and compare the 3D microstructures of the cathode samples.

*Volume fraction.* A fundamental microstructure descriptor is the volume fraction of a predefined phase. It is estimated from voxelized image data by the ratio of the number of voxels assigned to the respective phase divided by the total number of voxels within the observation window [28]. Similar to [18], we also consider the distribution of local volume fraction. For this purpose, the observation window is subdivided into smaller parts, whose size is 50 voxels, both, in  $x$ - and  $y$ -direction. This allows us to characterize the local heterogeneity of the 3D microstructure.

*Specific surface area.* Another important microstructure descriptor is the specific surface area  $A$  of a certain phase, which is defined as the ratio of the surface area of the phase divided by the volume of the observation window. An estimator for  $A$  can be computed from voxelized image data by means of differently weighted  $2 \times 2 \times 2$  voxel configurations, using the weights proposed in [66].

*Continuous phase size distribution.* A further important microstructure descriptor is the continuous phase size distribution  $\text{CPSD} : [0, \infty) \rightarrow [0, 1]$ . For any  $r \in [0, \infty)$ , the value  $\text{CPSD}(r)$  is defined as the fraction of a considered phase, which can be filled using spheres with radius  $r$ . Those balls can overlap, but are not allowed to intersect with the complementary phase. The 2D examples shown in Figure S1 illustrate this idea. To estimate the continuous pore size distribution from voxelized image data, the method described in [67] was used.

*Simulated mercury intrusion porosimetry.* The simulated mercury intrusion porosimetry, denoted by  $\text{MIP} : [0, \infty) \rightarrow [0, 1]$ , is based on the same principle as the continuous phase size distribution described above, but in contrast to  $\text{CPSD}$  an intrusion of the considered phase from a certain direction is simulated. Therefore, the value of  $\text{MIP}(r)$  is given by the fraction of the considered phase which can be filled by infiltrating it from a given side (i.e., in our case, from the separator) using spheres with radius  $r$ . As the name suggests, it is basically a simulated version of the experimental technique called mercury intrusion porosimetry, which is frequently used to experimentally characterize the microstructure of porous materials [68, 69]. Because of the added directional restriction, the presence of bottlenecks as well as the connectedness of the considered phase both have a major impact on  $\text{MIP}$ , in contrast to  $\text{CPSD}$ , see Figure S2. The estimation of  $\text{MIP}$  from voxelized image data is carried out as described in [70].

*Constrictivity.* Based on  $\text{CPSD}$  and  $\text{MIP}$ , it is possible to quantify bottleneck effects in a phase using the notion of constrictivity which is defined as  $\beta = \left(\frac{r_{\min}}{r_{\max}}\right)^2$  [67]. The values  $r_{\min} \geq 0$  and  $r_{\max} \geq 0$  are solutions of the equations  $\text{MIP}(r_{\min}) = 0.5$  and  $\text{CPSD}(r_{\max}) = 0.5$ , respectively. It is clear that  $\text{MIP}(r) \leq \text{CPSD}(r)$  holds for any  $r \geq 0$ . Thus,  $r_{\min} \leq r_{\max}$  and, therefore,  $\beta \in [0, 1]$ . Note that a value of  $\beta$  close to one indicates a near perfect connectivity of the considered phase without any significant constrictions. On the other hand, a value close to zero implies that there are strong bottlenecks, which considerably restrict transport along the specified direction [71, 70, 72].

*Geodesic tortuosity.* Usually, the mean geodesic tortuosity  $\tau \geq 1$  of a material’s phase is defined as the mean value of the distribution of shortest path lengths through this phase starting from a certain predefined plane towards some (parallel) target plane, divided by the distance between those two planes. This direction-dependent geometric quantity is closely related to effective properties of the considered phase [70, 71]. Note, however, that there exist different concepts of tortuosity in the literature [73, 74, 75]. In the present paper, besides the mean value  $\tau$ , we also consider the distribution of shortest path lengths, where the shortest paths have been computed in through-plane direction, i.e., in other words, from any point of the considered phase towards the “separator side”. For this purpose, Dijkstra’s algorithm is used [76]. The result obtained by this well-known algorithm is what we refer to as the shortest distance image in the following. In this image, the shortest quasi-Euclidean distance to the separator is assigned to each voxel within the considered phase, which is connected to the separator by a path within the predefined phase. This shortest distance image will be used as a basis for quantitatively analyzing shortest paths as a function of their location within the electrode. More precisely, we consider the plane  $p_d$ , which is parallel to the separator, with distance  $d > 0$  to the separator. This allows us to consider the average length of shortest paths from the plane  $p_d$  to the separator divided by  $d$ , which will be denoted by  $\tau_d$ . In particular, the mean geodesic tortuosity  $\tau$  mentioned at the beginning of this paragraph corresponds to  $\tau_d$  if  $d$  equals the electrode thickness. In Figure S3, 2D examples for two different

positions of  $p_d$  in a shortest distance image and the corresponding shortest paths are shown. In addition, a more formal discussion of the concept of geodesic tortuosity within the framework of random closed sets can be found in [77].

#### 4.2. Particle-based descriptors

Active particles of battery electrodes play a major role during the dis-/charging process. Moreover, in the present study, particle-based microstructure descriptors are of particular interest as the underlying raw material is identical for all three sample sets. Possible differences in particle morphologies can only arise due to different specifications of production parameters.

*Volume-equivalent radius.* Since the active particles of our sample sets are nearly spherical, a suitable approach to compare the particle sizes across all samples is to consider the distribution of volume-equivalent radii, i.e., the radii of perfect spheres with the same volume as the respective particles.

*Sphericity.* The sphericity, first proposed in [78], is a measure quantifying the deviation of the shape of a certain object from that of a perfect sphere. It is defined as

$$\psi = \frac{\sqrt[3]{\pi}(6V)^{2/3}}{S},$$

where  $S$  and  $V$  denote the surface area and the volume of the particle, respectively. This quantity is computed for each particle leading to the distribution of sphericity, where larger values of  $\psi$  correspond to more spherical particles.

*Coordination number.* Finally, the connectivity of the system of active particles is considered. It will be quantitatively described by the distribution of coordination numbers, i.e., the distribution of the number of neighbors directly connected to any particle within the system of active particles.

## 5. Results

We now present the results obtained from the analysis and quantitative comparison of the 3D microstructures of the three cathode sample sets, in order to highlight the advantages and disadvantages of increasing cathode thickness as well as different degrees of compaction. In particular, we will investigate possible benefits of structured two-layer cathodes compared to conventional single-layer electrodes. This will be done with respect to both phase-based and particle-based descriptors.

### 5.1. Phase-based descriptors of single- and two-layer cathodes

*Volume fraction.* Obviously, a higher compaction load leads to a higher (global) volume fraction of active material, see Figure 3. Furthermore, the variance of local porosity and, in turn, the variance of local volume fraction of active material is smaller for samples manufactured with higher compaction loads. We suppose that this decrease is mainly due to the fact that especially large pores are filled with active material when the compaction load is increased. Note that there are only slight variations of the maximum local volume fraction of active material within sample set B, whereas this quantity increases by around 20% for sample set A. In contrast to that, the maximum

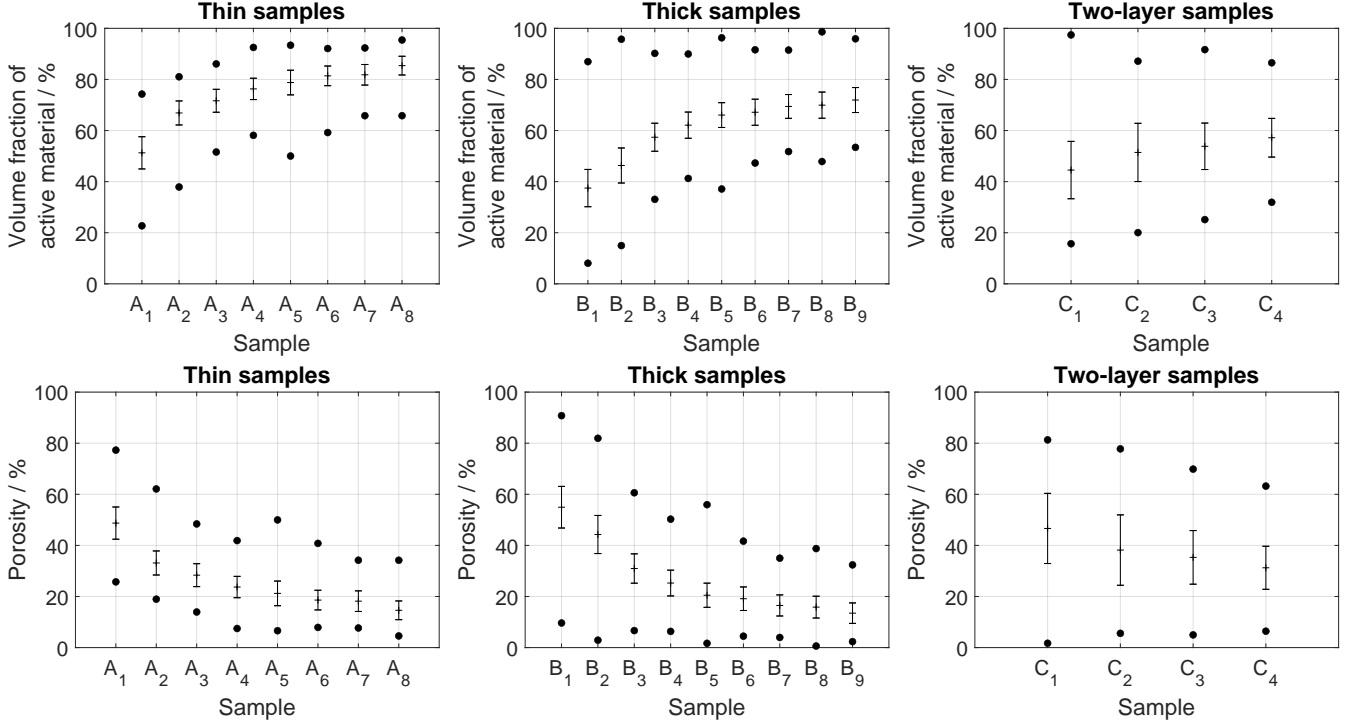


Figure 3: Local volume fraction of active material (top) and local porosity (bottom) of all three sample sets visualized by their mean (dash), standard deviation (error bar) and minimum as well as maximum (dots) for increasing compaction load.

local porosity is significantly decreasing for all sample sets as the compaction load increases. With regard to sample set A, this quantity is reduced by around 40%, and for sample set B even by around 60%. Thus, a higher compaction load not only leads to a higher mean volume fraction of active material but also creates a less heterogeneous microstructure in single-layer electrodes. These changes in heterogeneity are especially pronounced for low compaction loads. At some point, however, that behavior changes and the impact of higher compaction loads on standard deviation diminishes, similar to the mean values of local porosity and local volume fraction of active material. This indicates that already relatively low compaction loads create microstructures, where nearly all large pores are filled and active particles are confined to their positions. The two-layer sample set behaves differently. Presumably due to their two-layer structure, the morphology of the two-layer samples is relatively heterogeneous in terms of larger standard deviations of local volume fractions. For example, the local porosity of sample C<sub>4</sub> has a standard deviation of around 8.4%, while the local porosity of sample B<sub>3</sub> (with a similar thickness and mean porosity) only has a standard deviation of around 5.7%.

*Specific surface area.* The specific surface area of active material is a further relevant microstructure descriptor. By increasing the compaction load, two contrary trends can be observed. On the one hand, the densification of active material leads to larger contact areas between active particles, which reduces the surface area of active material. On the other hand, the higher the compaction load the smaller the volume in the denominator of the definition of  $A$  (due to the decrease in sam-

sample number	1	2	3	4	5	6	7	8	9
<b>sample set A</b>									
$A/\text{mm}^{-1}$	268	318	342	348	338	344	336	332	
<b>sample set B</b>									
$A/\text{mm}^{-1}$	239	276	310	327	318	326	318	314	311
<b>sample set C</b>									
$A/\text{mm}^{-1}$	236	267	269	281					

Table 3: Specific surface area of active material for the sample sets A, B and C.

ple thickness), leading to an increase of specific surface. With regard to sample sets A and B, the latter trend can be observed at low compaction loads, whereas for higher degrees of densification the increase in contact area is the main influencing factor, see Table 3. With regard to sample set C, the specific surface area is monotonously increasing since it is dominated by the decreasing volume of the observation window.

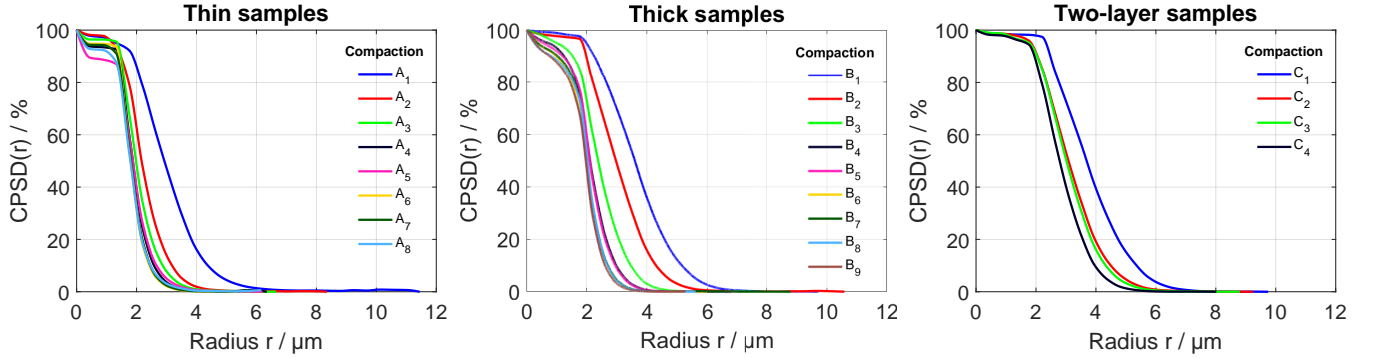


Figure 4: Continuous pore size distribution of sample sets A (left), B (center) and C (right).

*Continuous pore size distribution.* The continuous pore size distribution, i.e., the continuous phase size distribution of pore space, shown in Figure 4, supports the observations described above: the rate of changes is diminishing for higher compaction loads. In general, sample set A seems to exhibit larger pores compared to the other two sample sets, since  $r_{\max}$  declines from  $5.8\ \mu\text{m}$  to  $3.6\ \mu\text{m}$  (for sample set A) compared to a decrease from  $3.6\ \mu\text{m}$  to  $2\ \mu\text{m}$  (for sample set B) and from  $3.7\ \mu\text{m}$  to  $2.8\ \mu\text{m}$  (for sample set C). But, apart from this behavior, the general trend is the same for all three sample sets. In particular, there is a significant shift of the CPSD to the left between samples  $A_1$  and  $A_4$ ,  $B_1$  and  $B_4$  as well as  $C_1$  and  $C_2$ , whereas the continuous pore size distribution is only subject to minor changes in the regime of higher compaction loads. However, a closer look at the simulated mercury intrusion porosimetry considered below will reveal that higher compaction loads still significantly change the 3D microstructure.

*Simulated mercury intrusion porosimetry.* As can be seen in the plots shown in Figure 5, the curves of simulated mercury intrusion porosimetry are shifted to the left when increasing the compaction

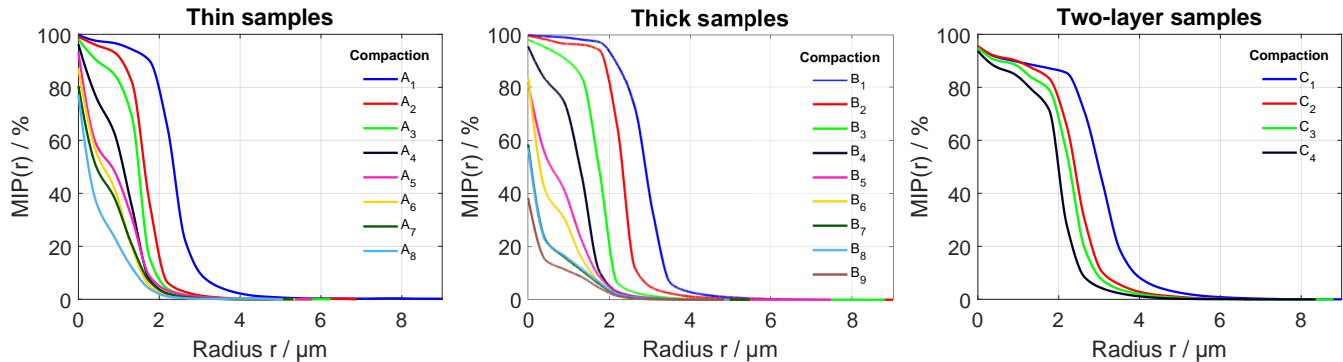


Figure 5: Simulated mercury intrusion porosimetry of pore space for the sample sets A (left), B (center) and C (right).

load, which holds for all three sample sets. In particular, the curves of sample set B show a steep drop right at the beginning, which corresponds to a relatively large volume that can not be reached at all by an intrusion from the separator. In the extreme case of  $B_9$ , only 38% of the pore space can be reached in this way, i.e., 62% of the pore space consist of isolated clusters not connected to the starting plane. In addition, more pronounced bottlenecks occur in the thick cathode samples, which can be observed, e.g., for intruding spheres with a radius of about  $3\ \mu\text{m}$ . In this domain, all curves corresponding to compacted thick samples are close to zero, whereas a significant volume of the pore space can be reached by such intruding spheres when considering the thin samples. This not only shows the impact of cathode thickness on the transport paths through the pore space, but also that high compaction loads further hinder transport within the pore space, even though such effects are less pronounced with respect to the CPSD. What is especially interesting, however, is the comparison of sample sets B and C with respect to MIP. Namely, the comparison of samples  $C_4$  and  $B_3$ , which have similar thicknesses and similar mean porosities, shows more desirable transport properties for the pore phase of sample  $C_4$  compared to those of sample  $B_3$ . While the curve of CPSD already indicates that  $C_4$  tends to have larger pores compared to  $B_3$ , the curve of MIP shows that they are also slightly better connected. For sample  $C_4$ , the bottleneck radius  $r_{\min}$  equals  $2\ \mu\text{m}$ , and spheres with radius  $r = 4\ \mu\text{m}$  can still fill a small portion of its pore space, whereas  $r = 3.5\ \mu\text{m}$  is too large to fill any part of the pore space of sample  $B_3$ , for which it holds that  $r_{\min} = 1.76\ \mu\text{m}$ .

sample number	1	2	3	4	5	6	7	8	9
<b>sample set A</b>									
$\beta$	0.645	0.566	0.561	0.349	0.195	0.114	0.059	0.019	
<b>sample set B</b>									
$\beta$	0.647	0.613	0.538	0.367	0.072	0.021	0.001	0.001	0
<b>sample set C</b>									
$\beta$	0.656	0.604	0.565	0.510					

Table 4: Constrictivity of pore space for the sample sets A, B and C.

*Constrictivity.* The values for the constrictivity of pore space, shown in Table 4, clearly indicate that the samples  $A_1$  to  $A_4$  and their respective counterparts  $B_1$  to  $B_4$  have similar constrictivities, which are decreasing for increasing compaction loads. However, the thick cathodes of sample set B show more pronounced bottleneck effects in case of highly densified samples compared to sample set A. In particular, the constrictivity decreases significantly from  $B_4$  to  $B_5$  and decreases even further to almost zero for  $B_6$  to  $B_8$ , which is caused by the steep drop of the values  $MIP(r)$  of MIP for small  $r > 0$ , thus leading to small values of  $r_{min}$ . Sample  $B_9$  is a specific case, since less than 50% of the pore phase is connected to the separator leading to  $\beta = 0$ . As expected, the constrictivity is decreasing with increasing compaction load with regard to the two-layer electrodes. In addition, the range of these constrictivity values is comparable to the other two sample sets when considering only electrodes with similar porosities.

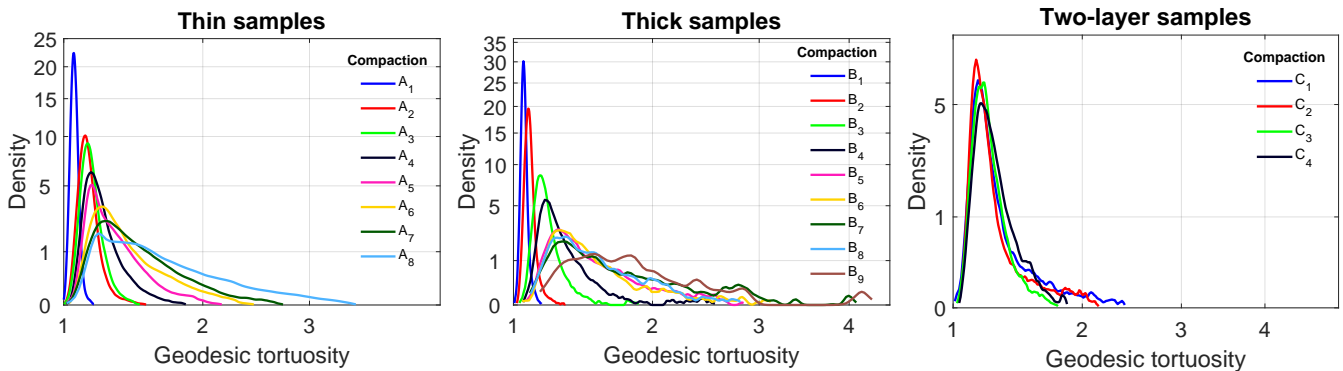


Figure 6: Probability density of the geodesic tortuosity of pore phase for the sample sets A (left), B (center) and C (right). Note the square root scaling of both axes for visualization purposes.

*Geodesic tortuosity.* For all three sample sets, the densities of geodesic tortuosity are clearly shifted to the right with increasing compaction load, as can be seen in Figure 6. Additionally, they become successively more right skewed for an increasing level of densification, *i.e.*, the relative number of shortest paths with exceptionally large lengths is increasing disproportionately. While the values of geodesic tortuosity are always smaller than 1.5 for the uncompacted samples, the samples  $A_6$  and  $B_5$  contain a considerable amount of shortest paths which are twice as long as the respective sample thickness. Furthermore, the differences in the distribution of geodesic tortuosity for samples from sample set C are small, indicating that the main influence factor on this distribution is the highly compacted layer close to the current collector.

Note that, for the densified samples, the quantity  $\tau_d$  takes its maximum for values of  $d$  in the first third of sample thickness, as can be seen in Figure 7. In particular, this effect is even more pronounced for highly compacted electrodes. A closer look at their shortest distance images reveals that, in this case, there exist a considerable number of pore voxels close to the separator, from which the separator can only be reached by paths traversing large parts of the cathode. This effect is visualized in the bottom plot of Figure S3. In combination with a relatively small distance  $d$  to the separator, this leads to a high mean geodesic tortuosity  $\tau_d$  in the first third of sample thickness. Furthermore, for the highly compacted samples in sample set B of thick cathodes, numerous pore voxels in starting planes with a large distance  $d$  to the separator are not connected to the target plane at all, which leads to the large oscillations of the curves in Figure 7 corresponding

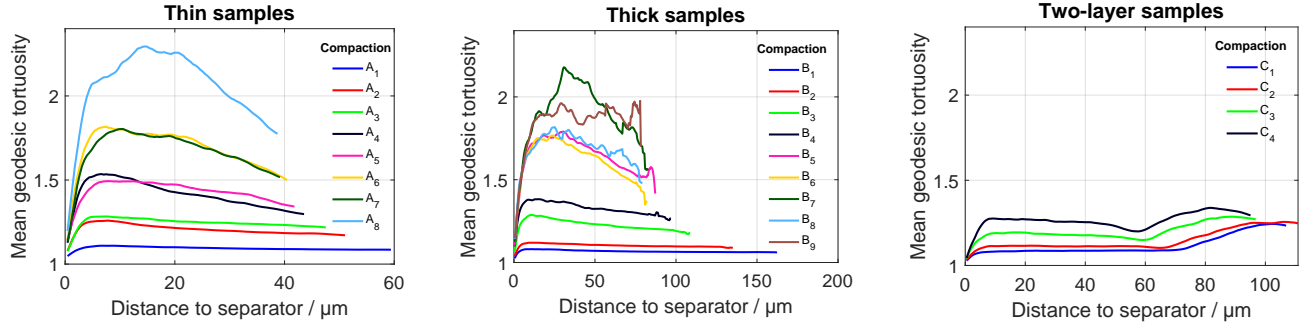


Figure 7: Distance-dependent mean geodesic tortuosity  $\tau_d$  for the sample sets A (left), B (center) and C (right).

to the samples  $B_7$ ,  $B_8$  and  $B_9$ . This also explains why some less compacted samples partially have larger values of  $\tau_d$  compared to their more compressed counterparts. For example, the distance-dependent mean geodesic tortuosity  $\tau_d$  of sample  $B_7$  is in parts larger compared to the values of  $\tau_d$  for sample  $B_9$ . The decrease of the percentage of pore voxels connected to the separator with increasing distance  $d$  to it is quantitatively visualized in Figure 8.

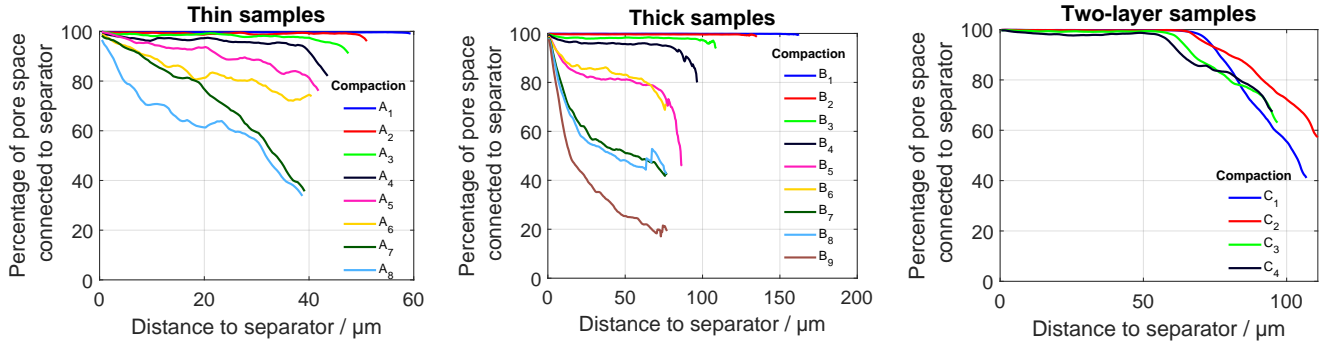


Figure 8: Percentage of pore voxels connected to the separator as a function of distance  $d$  for the sample sets A (left), B (center) and C (right).

## 5.2. Particle-based descriptors of single- and two-layer cathodes

*Volume-equivalent radius.* The particle size distributions are similar for all samples, see Figure 9. In particular, they are similar to each other for all compaction loads of a given sample set, i.e., particle breakage is not an issue. With regard to sample set A, there seems to be a small trend towards smaller particles, while for sample sets B and C the opposite is true. These minor differences are likely caused by the choice of parameters during particle-based segmentation and are therefore negligible.

*Sphericity.* In contrast to the behavior of the particle size distribution described above, the observed changes of sphericity are much more pronounced, see Figure 10. In particular, when considering the transition from sample  $A_2$  to  $A_3$ , the probability density of sphericity is clearly shifted to the left, i.e., to less spherical particles. On the other hand, for sample set B, the sphericity distributions change more gradually towards less spherical particles. For the four samples of sample set C, there is only a minor shift of the densities of particle sphericity to the left with decreasing porosity

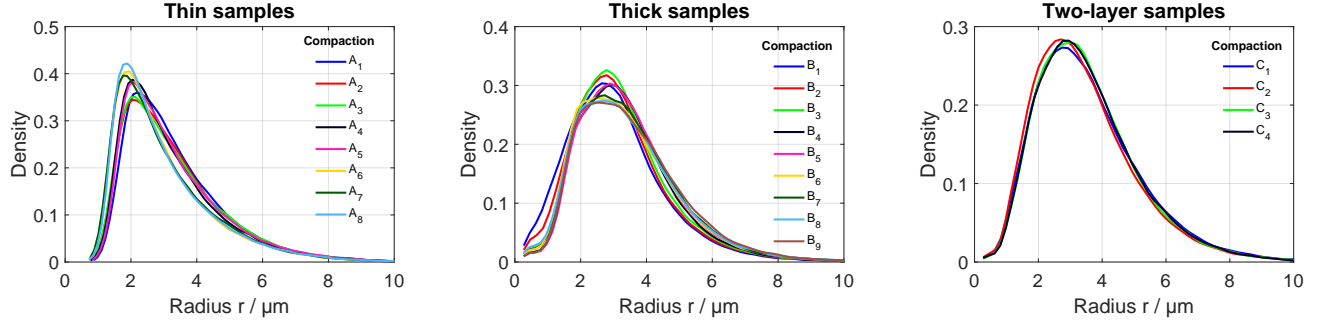


Figure 9: Probability density of volume-equivalent particle radii for sample sets A (left), B (center) and C (right).

of the top layer. Thus, the changes in sphericity in combination with the particle size distribution, which is not influenced by the compaction load, suggest that the active material particles are being noticeably deformed, but do not break.

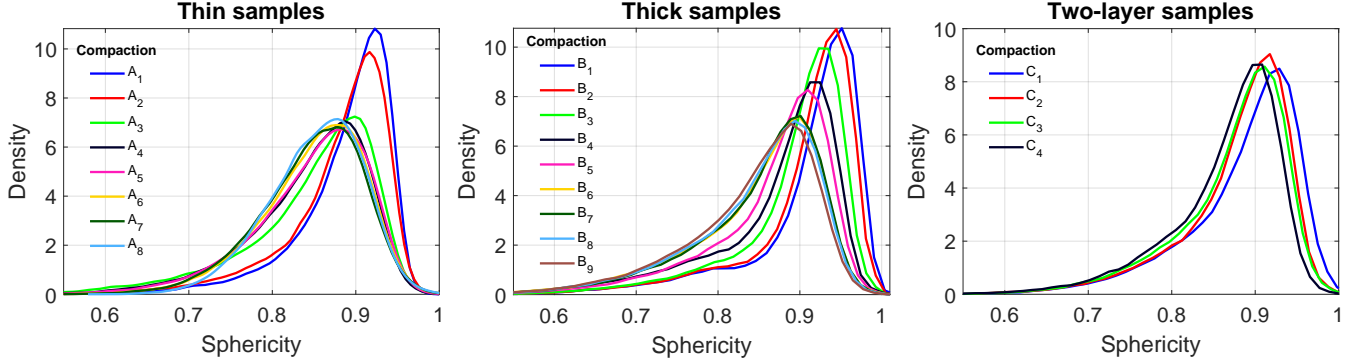


Figure 10: Probability density of particle sphericity for sample sets A (left), B (center) and C (right).

*Coordination number.* The connectivity of the system of active particles described by their coordination numbers shows the same kind of behavior as, for example, the CPSD for all sample sets, see Figure 11. More precisely, the changes of the sample morphologies are more pronounced in case of low compaction loads, whereas a higher degree of densification only leads to minor additional structural changes. The shift of the distribution functions of the coordination number to the right, which corresponds to an increase of connectivity, is most distinct between samples  $A_1$  to  $A_3$  and significantly decreases between samples  $A_4$  and  $A_8$  as well as between  $B_4$  and  $B_9$ . With regard to sample set C, there are only minor changes in the distribution of coordination numbers across all four samples.

### 5.3. In-depth analysis of two-layer cathodes

The results presented so far in Section 5 seem to indicate that there is indeed an advantage in using two-layer cathodes. In the following, we further investigate in which sense two-layer cathodes could be preferable compared to their counterparts with just one thick layer of coating. For this, we consider more detailed microstructure descriptors which depend on the distance to the interface between both layers, see also [53].

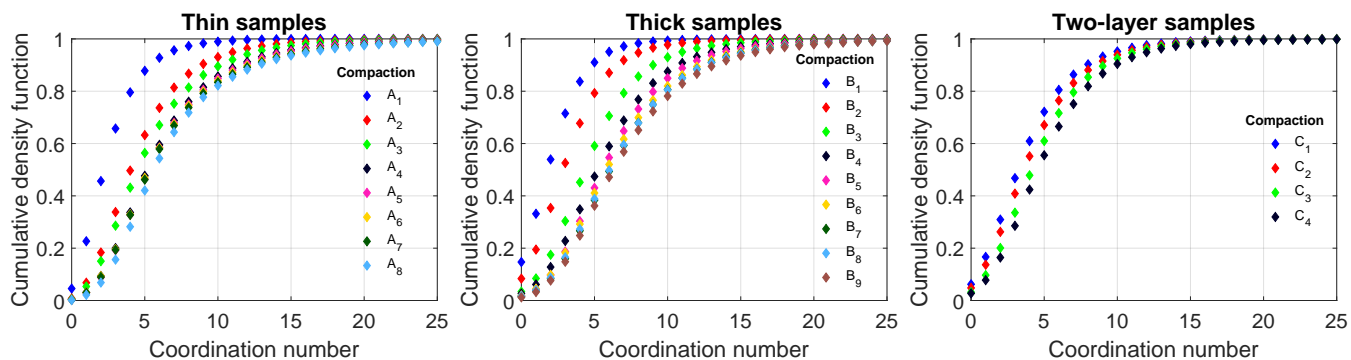


Figure 11: Cumulative distribution function of the coordination number of active particles for sample sets A (left), B (center) and C (right).

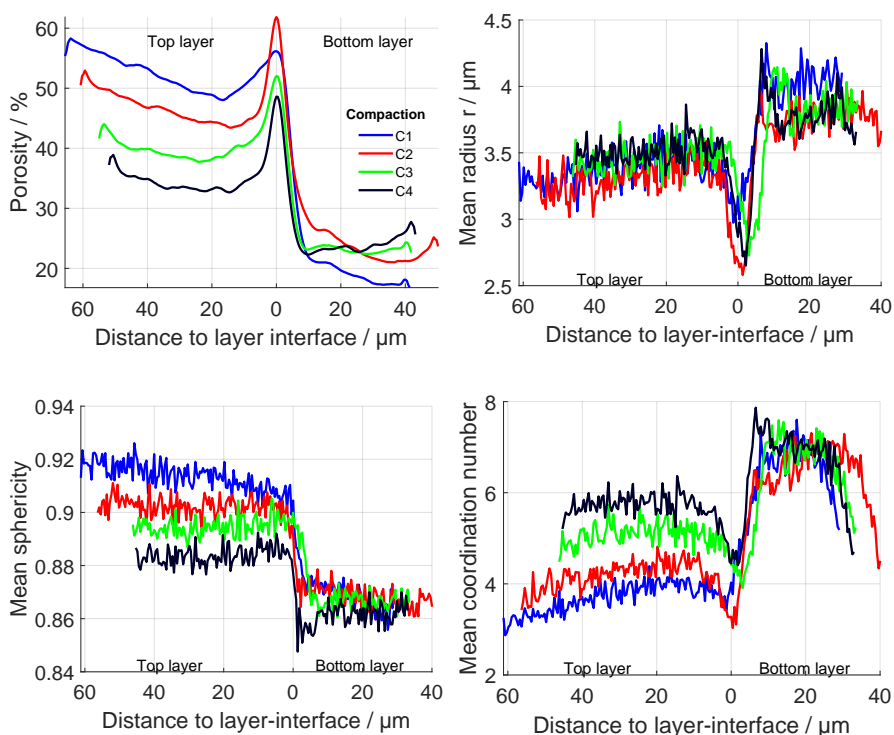


Figure 12: Distance-dependent porosity (top left), mean volume-equivalent particle radius (top right), mean sphericity (bottom left) and mean coordination number (bottom right) for the two-layer electrodes (sample set C).

Note that the interface between both layers is clearly discernible, when considering the microstructure descriptors shown in Figure 12. All four two-layer samples of sample set C exhibit a distance interval around the interface where the porosity increases by 5% to 10%. This has, of course, an effect on the mean coordination number, which drops significantly in that region. Furthermore, a drop in particle size is observed near the interface. Since the positions of particle centers are chosen to compute the distances of particles to the interface and the increase of porosity at the interface indicates that the number of particles crossing the interface into the other layer is relatively small, a large fraction of radii of particles close to the interface have to be equal or smaller than the distances of the corresponding particle centers to the interface. Note that particles that

are either close to the current collector or the separator are excluded from the above analysis of distance-dependent characteristics to keep the plots clear. Another interesting observation is that the porosity of the bottom layer is smaller than expected. Instead of having a porosity of around 30%, it seems to be between 20% and 25%. Even for sample C<sub>4</sub> such unexpected values of distance-dependent porosities of the bottom layer are obtained. Furthermore, there is a substantial decrease in sphericity and an increase in connectivity when passing from top to bottom layer. These findings for the region around the interface between the two layers are presumably the reason why charge transport in sample set C seems to be less hindered than in the one-layer samples of sample set B with comparable thickness. When looking at the distance-dependent mean geodesic tortuosity  $\tau_d$  of pore space, the increased porosity around the interface between the two layers appears to act like a reset point because of which ionic transport properties of both layers have nearly no influence on each other. In other words, to a certain extent the transportation paths in the top layer seem to be independent of the paths in the bottom layer. More precisely, transportation paths within the top layer which are separated from one another can reconnect in the interface between both layers, thereby mitigating some of those transportation restrictions. This would make two-layer cathodes preferable compared to single-layer cathodes with similar thickness. However, the decrease in particle connectivity near the interface could have an adverse effect on the electric transport within the active material phase of two-layer cathodes.

## 6. Conclusions

Three sets of differently manufactured cathodes have been measured by means of synchrotron tomography. The first sample set consisted of eight differently compacted thin electrodes, whereas the second sample set contained nine thick cathodes with varying degree of densification. In addition, a set of four two-layer cathodes with varying porosities in the top layer has been considered. The resulting 3D image data has been segmented into active material, binder and pores, which was followed by a particle-based segmentation based on the watershed algorithm. The segmented image data allows to quantify the influence of the compaction load on the electrode morphology as well as a microstructural comparison between thin, thick and two-layer cathodes by means of transport-relevant phase- and particle-based descriptors.

In particular, the processed 3D image data allows us to extract valuable information about the cathode morphology, which can not be obtained by 2D image data or experimental approaches. In general, there are microstructure characteristics which are not significantly influenced by the compaction load, as, for example, the particle size distribution. On the other hand, there are certain descriptors of 3D microstructure that strongly depend on the compaction load, as, for example, the volume fraction of active material. But, while the changes of some quantities are more pronounced between samples produced with low compaction loads, other characteristics change mainly between samples with a high level of compression. In addition, it turned out that, beginning from a certain point, further increasing the thickness or the compaction load can considerably reduce the connectivity of the pore phase, which results in an increasing amount of disconnected pore regions. Moreover, this leads to an increasing fraction of active material with diminished accessibility, which can not be dis-/charged effectively. Therefore, increasing the coating thickness or the compaction load to raise the electrode capacity has its limitations. However, it has been shown that two-layer cathodes have the potential to bypass some of those limitations, at least with regard to the

pore space. The interface between both layers seems to act like a kind of reset point for possible transportation paths through the electrodes, which indicates that ionic transport seems to be less restricted for two-layer cathodes compared to one-layered cathodes with similar thickness and porosity. These results indicate that future battery research should, among others, be targeted towards two-layer electrodes to further optimize the electrochemical performance of lithium-ion batteries.

### Data availability

The raw/processed data required to reproduce these findings cannot be shared at this time as the data also forms part of another ongoing study.

### References

- [1] B. Scrosati, K. M. Abraham, W. van Schalkwijk, and J. Hassoun, eds., Lithium Batteries: Advanced Technologies and Applications. Hoboken: J. Wiley & Sons, 2013.
- [2] G. Nazri and G. Pistoia, Lithium Batteries: Science and Technology. New York: Springer, 2<sup>nd</sup> ed., 2008.
- [3] G. E. Blomgren, “The development and future of lithium ion batteries,” Journal of The Electrochemical Society, vol. 164, no. 1, p. A5019–A5025, 2016.
- [4] J. B. Goodenough and K.-S. Park, “The Li-ion rechargeable battery: A perspective,” Journal of the American Chemical Society, vol. 135, no. 4, p. 1167–1176, 2013.
- [5] H. D. Yoo, E. Markevich, G. Salitra, D. Sharon, and D. Aurbach, “On the challenge of developing advanced technologies for electrochemical energy storage and conversion,” Materials Today, vol. 17, no. 3, p. 110–121, 2014.
- [6] R. Korthauer, Lithium-Ion Batteries: Basics and Applications. Berlin: Springer, 2018.
- [7] J. R. Wilson, J. S. Cronin, S. A. Barnett, and S. J. Harris, “Measurement of three-dimensional microstructure in a LiCoO<sub>2</sub> positive electrode,” Journal of Power Sources, vol. 196, no. 7, p. 3443–3447, 2011.
- [8] S. Cho, C.-F. Chen, and P. P. Mukherjee, “Influence of microstructure on impedance response in intercalation electrodes,” Journal of The Electrochemical Society, vol. 162, no. 7, p. A1202–A1214, 2015.
- [9] X. Huang, J. Tu, X. Xia, X. Wang, J. Xiang, L. Zhang, and Y. Zhou, “Morphology effect on the electrochemical performance of NiO films as anodes for lithium ion batteries,” Journal of Power Sources, vol. 188, no. 2, p. 588–591, 2009.
- [10] G. Lenze, H. Bockholt, C. Schilcher, L. Froböse, D. Jansen, U. Krewer, and A. Kwade, “Impacts of variations in manufacturing parameters on performance of lithium-ion batteries,” Journal of The Electrochemical Society, vol. 165, no. 2, p. A314–A322, 2018.

- [11] W. Li and J. C. Currie, “Morphology effects on the electrochemical performance of  $\text{LiNi}_{1-x}\text{Co}_x\text{O}_2$ ,” Journal of The Electrochemical Society, vol. 144, no. 8, p. 2773–2779, 1997.
- [12] Y. Shin and A. Manthiram, “Influence of microstructure on the electrochemical performance of  $\text{LiMn}_{2-y-z}\text{Li}_y\text{Ni}_z\text{O}_4$  spinel cathodes in rechargeable lithium batteries,” Journal of Power Sources, vol. 126, no. 1, p. 169–174, 2004.
- [13] A. H. Wiedemann, G. M. Goldin, S. A. Barnett, H. Zhu, and R. J. Kee, “Effects of three-dimensional cathode microstructure on the performance of lithium-ion battery cathodes,” Electrochimica Acta, vol. 88, p. 580–588, 2013.
- [14] J. E. Vogel, M. M. Forouzan, E. E. Hardy, S. T. Crawford, D. R. Wheeler, and B. A. Mazzeo, “Electrode microstructure controls localized electronic impedance in Li-ion batteries,” Electrochimica Acta, vol. 297, p. 820–825, 2019.
- [15] P. R. Shearing, N. P. Brandon, J. Gelb, R. Bradley, P. J. Withers, A. J. Marquis, S. Cooper, and S. J. Harris, “Multi length scale microstructural investigations of a commercially available li-ion battery electrode,” Journal of The Electrochemical Society, vol. 159, p. A1023–A1027, 2012.
- [16] M. Ebner, F. Geldmacher, F. Marone, M. Stampanoni, and V. Wood, “X-ray tomography of porous, transition metal oxide based lithium ion battery electrodes,” Advanced Energy Materials, vol. 3, p. 845–850, 2013.
- [17] T. Mitsch, Y. Krämer, J. Feinauer, G. Gaiselmann, H. Markötter, I. Manke, A. Hintennach, and V. Schmidt, “Preparation and characterization of li-ion graphite anodes using synchrotron tomography,” Materials, vol. 7, p. 4455–4472, 2014.
- [18] K. Kuchler, B. Priffling, D. Schmidt, H. Markötter, I. Manke, T. Bernthaler, V. Knoblauch, and V. Schmidt, “Analysis of the 3D microstructure of experimental cathode films for lithium-ion batteries under increasing compaction,” Journal of Microscopy, vol. 272, no. 2, p. 96–110, 2018.
- [19] B. Priffling, A. Ridder, A. Hilger, M. Osenberg, I. Manke, K. P. Birke, and V. Schmidt, “Analysis of structural and functional aging of electrodes in lithium-ion batteries during rapid charge and discharge rates using synchrotron tomography,” Journal of Power Sources, vol. 443, p. 227259, 2019.
- [20] H. Bockholt, M. Indrikova, A. Netz, F. Golks, and A. Kwade, “The interaction of consecutive process steps in the manufacturing of lithium-ion battery electrodes with regard to structural and electrochemical properties,” Journal of Power Sources, vol. 325, p. 140–151, 2016.
- [21] L. S. Kremer, A. Hoffmann, T. Danner, S. Hein, B. Priffling, D. Westhoff, C. Dreer, A. Latz, V. Schmidt, and M. Wohlfahrt-Mehrens, “Manufacturing process for improved ultra-thick cathodes in high-energy lithium-ion batteries,” Energy Technology, vol. 8, no. 2, p. 1900167, 2020.

- [22] H. Bockholt, W. Haselrieder, and A. Kwade, “Intensive dry and wet mixing influencing the structural and electrochemical properties of secondary lithium-ion battery cathodes,” ECS Transactions, vol. 50, p. 25–35, 2013.
- [23] F. Huttner, W. Haselrieder, and A. Kwade, “The influence of different post-drying procedures on remaining water content and physical and electrochemical properties of lithium-ion batteries,” Energy Technology, vol. 8, no. 2, p. 1900245, 2020.
- [24] J. Kumberg, M. Baunach, J. C. Eser, A. Altvater, P. Scharfer, and W. Schabel, “Investigation of drying curves of lithium-ion battery electrodes with a new gravimetric double-side batch dryer concept including setup characterization and model simulations,” Energy Technology, vol. 9, no. 2, p. 2000889, 2021.
- [25] H. Zheng, L. Tan, G. Liu, X. Song, and V. S. Battaglia, “Calendering effects on the physical and electrochemical properties of  $\text{Li}[\text{Ni}_{1/3}\text{Mn}_{1/3}\text{Co}_{1/3}]\text{O}_2$  cathode,” Journal of Power Sources, vol. 208, p. 52–57, 2012.
- [26] W. Haselrieder, S. Ivanov, D. K. Christen, H. Bockholt, and A. Kwade, “Impact of the calendering process on the interfacial structure and the related electrochemical performance of secondary lithium-ion batteries,” ESC Transactions, vol. 50, no. 26, p. 59–70, 2013.
- [27] B. Prifling, D. Westhoff, D. Schmidt, H. Markötter, I. Manke, V. Knoblauch, and V. Schmidt, “Parametric microstructure modeling of compressed cathode materials for Li-ion batteries,” Computational Materials Science, vol. 169, p. 109083, 2019.
- [28] S. N. Chiu, D. Stoyan, W. S. Kendall, and J. Mecke, Stochastic Geometry and its Applications. Chichester: J. Wiley & Sons, 3<sup>rd</sup> ed., 2013.
- [29] C. Lantuejoul, Geostatistical Simulation: Models and Algorithms. Berlin: Springer, 2013.
- [30] M. Singh, J. Kaiser, and H. Hahn, “Thick electrodes for high energy lithium ion batteries,” Journal of The Electrochemical Society, vol. 162, no. 7, p. A1196–A1201, 2015.
- [31] J. S. Wang, P. Liu, E. Sherman, M. Verbrugge, and H. Tataria, “Formulation and characterization of ultra-thick electrodes for high energy lithium-ion batteries employing tailored metal foams,” Journal of Power Sources, vol. 196, no. 20, p. 8714–8718, 2011.
- [32] H. Zheng, J. Li, X. Song, G. Liu, and V. S. Battaglia, “A comprehensive understanding of electrode thickness effects on the electrochemical performances of Li-ion battery cathodes,” Electrochimica Acta, vol. 71, p. 258–265, 2012.
- [33] H. Abe, M. Kubota, M. Nemoto, Y. Masuda, Y. Tanaka, H. Munakata, and K. Kanamura, “High-capacity thick cathode with a porous aluminum current collector for lithium secondary batteries,” Journal of Power Sources, vol. 334, p. 78–85, 2016.
- [34] Z. Du, D. Wood, C. Daniel, S. Kalnaus, and J. Li, “Understanding limiting factors in thick electrode performance as applied to high energy density Li-ion batteries,” Journal of Applied Electrochemistry, vol. 47, p. 405–415, 2017.

- [35] T. Danner, M. Singh, S. Hein, J. Kaiser, H. Hahn, and A. Latz, "Thick electrodes for Li-ion batteries: A model based analysis," Journal of Power Sources, vol. 334, p. 191–201, 2016.
- [36] D. L. Wood, J. Li, and C. Daniel, "Prospects for reducing the processing cost of lithium ion batteries," Journal of Power Sources, vol. 275, p. 234–242, 2015.
- [37] J. Kang, Y. Jia, G. Zhu, J. V. Wang, B. Huang, and Y. Fan, "How electrode thicknesses influence performance of cylindrical lithium-ion batteries," Journal of Energy Storage, vol. 46, p. 103827, 2022.
- [38] A. M. Boyce, D. J. Cumming, C. Huang, S. P. Zankowski, P. S. Grant, D. J. L. Brett, and P. R. Shearing, "Design of scalable, next-generation thick electrodes: Opportunities and challenges," ACS Nano, vol. 15, no. 12, p. 18624–18632, 2021.
- [39] J. Whitacre, K. Zaghbi, W. West, and B. Ratnakumar, "Dual active material composite cathode structures for Li-ion batteries," Journal of Power Sources, vol. 177, no. 2, p. 528–536, 2008.
- [40] K. Song, W. Li, Z. Chen, X. Wu, Q. Zhou, K. Snyder, and L. Zhang, "An effective approach to improve electrochemical performance of thick electrodes," Ionics, vol. 27, p. 1261–1270, 2021.
- [41] W. Ji, H. Qu, X. Zhang, D. Zheng, and D. Qu, "Electrode architecture design to promote charge-transport kinetics in high-loading and high-energy lithium-based batteries," Small Methods, vol. 5, no. 10, p. 2100518, 2021.
- [42] L. Liu, P. Guan, and C. Liu, "Experimental and simulation investigations of porosity graded cathodes in mitigating battery degradation of high voltage lithium-ion batteries," vol. 164, no. 13, p. A3163–A3173, 2017.
- [43] Y. Qi, T. Jang, V. Ramadesigan, D. T. Schwartz, and V. R. Subramanian, "Is there a benefit in employing graded electrodes for lithium-ion batteries?," Journal of The Electrochemical Society, vol. 164, no. 13, p. A3196–A3207, 2017.
- [44] W. Deng, W. Shi, Q. Liu, J. Jiang, X. Li, and X. Feng, "Constructing gradient porous structure in thick  $\text{Li}_4\text{Ti}_5\text{O}_{12}$  electrode for high-energy and stable lithium-ion batteries," ACS Sustainable Chemistry & Engineering, vol. 8, no. 46, p. 17062–17068, 2020.
- [45] C. Huang, M. Dontigny, K. Zaghbi, and P. S. Grant, "Low-tortuosity and graded lithium ion battery cathodes by ice templating," Journal of Materials Chemistry A, vol. 7, no. 37, p. 21421–21431, 2019.
- [46] C.-J. Bae, C. K. Erdonmez, J. W. Halloran, and Y.-M. Chiang, "Design of battery electrodes with dual-scale porosity to minimize tortuosity and maximize performance," Advanced Materials, vol. 25, no. 9, p. 1254–1258, 2013.
- [47] D. Schmidt, M. Kamlah, and V. Knoblauch, "Highly densified NCM-cathodes for high energy Li-ion batteries: Microstructural evolution during densification and its influence on the performance of the electrodes," Journal of Energy Storage, vol. 17, p. 213–223, 2018.

- [48] W. Görner, M. Hentschel, B. Müller, H. Rieseemeier, M. Krumrey, G. Ulm, W. Diete, U. Klein, and R. Frahm, “BAMline: the first hard X-ray beamline at BESSY II,” Nuclear Instruments and Methods in Physics Research Section A: Accelerators, Spectrometers, Detectors and Associated Equipment, vol. 467–468, p. 703–706, 2001. 7<sup>th</sup> International Conference on Synchrotron Radiation Instrumentation.
- [49] B. A. Dowd, G. H. Campbell, R. B. Marr, V. V. Nagarkar, S. V. Tipnis, L. Axe, and D. P. Siddons, “Developments in synchrotron X-ray computed microtomography at the National Synchrotron Light Source,” in Developments in X-Ray Tomography II (U. Bonse, ed.), vol. 3772, p. 224–236, International Society for Optics and Photonics, SPIE, 1999.
- [50] MATLAB, Version 9.4.0.813654 (R2018a). Natick, Massachusetts: The MathWorks Inc., 2018.
- [51] R. C. Gonzalez and R. E. Woods, Digital Image Processing. New York: Pearson, 4<sup>th</sup> ed., 2018.
- [52] J. C. Russ, The Image Processing Handbook. Boca Raton: CRC Press, 5<sup>th</sup> ed., 2007.
- [53] D. Westhoff, T. Danner, S. Hein, R. Scurtu, L. Kremer, A. Hoffmann, A. Hilger, I. Manke, M. Wohlfahrt-Mehrens, A. Latz, and V. Schmidt, “Analysis of microstructural effects in multi-layer lithium-ion battery cathodes,” Materials Characterization, vol. 151, p. 166–174, 2019.
- [54] W. Burger and M. Burge, Digital Image Processing: An Algorithmic Introduction Using Java. London: Springer, 2<sup>nd</sup> ed., 2016.
- [55] J. Hoshen and R. Kopelman, “Percolation and cluster distribution. I. Cluster multiple labeling technique and critical concentration algorithm,” Physical Review B, vol. 14, no. 8, p. 3438–3445, 1976.
- [56] E. Machado Charry, M. Neumann, J. Lahti, R. Schennach, V. Schmidt, and K. Zojer, “Pore space extraction and characterization of sack paper using  $\mu$ -CT,” Journal of Microscopy, vol. 272, no. 1, p. 35–46, 2018.
- [57] P. Soille, Morphological Image Analysis: Principles and Applications. New York: Springer, 2<sup>nd</sup> ed., 2003.
- [58] J. Serra, Image Analysis and Mathematical Morphology. London: Academic Press, 1982.
- [59] G. Matheron, Random Sets and Integral Geometry. New York: J. Wiley & Sons, 1975.
- [60] D. Kincaid and E. Cheney, Numerical Analysis: Mathematics of Scientific Computing. Providence: American Mathematical Society, 2009.
- [61] S. Hein, T. Danner, D. Westhoff, B. Prifling, R. Scurtu, L. Kremer, A. Hoffmann, A. Hilger, M. Osenberg, I. Manke, M. Wohlfahrt-Mehrens, V. Schmidt, and A. Latz, “Influence of conductive additives and binder on the impedance of lithium-ion battery electrodes: Effect of morphology,” Journal of The Electrochemical Society, vol. 167, no. 1, p. 013546, 2020.

- [62] J. B. Roerdink and A. Meijster, “The watershed transform: Definitions, algorithms and parallelization strategies,” Fundamenta Informaticae, vol. 41, p. 187–228, 2000.
- [63] S. Beucher and F. Meyer, “The morphological approach to segmentation: the watershed transformation,” in Mathematical Morphology in Image Processing (E. R. Dougherty, ed.), p. 433–481, New York: Marcel Dekker, Inc., 1993.
- [64] A. Spettl, R. Wimmer, T. Werz, M. Heinze, S. Odenbach, C. E. Krill III, and V. Schmidt, “Stochastic 3D modeling of Ostwald ripening at ultra-high volume fractions of the coarsening phase,” Modelling and Simulation in Materials Science and Engineering, vol. 23, no. 6, p. 065001, 2015.
- [65] K. Kuchler, D. Westhoff, J. Feinauer, T. Mitsch, I. Manke, and V. Schmidt, “Stochastic model for the 3D microstructure of pristine and cyclically aged cathodes in Li-ion batteries,” Modelling and Simulation in Materials Science and Engineering, vol. 26, no. 3, p. 035005, 2018.
- [66] K. Schladitz, J. Ohser, and W. Nagel, “Measuring intrinsic volumes in digital 3D images,” in 13th International Conference Discrete Geometry for Computer Imagery (A. Kuba, L. Nyúl, and K. Palágyi, eds.), (Berlin), p. 247–258, Springer, 2007.
- [67] B. Münch and L. Holzer, “Contradicting geometrical concepts in pore size analysis attained with electron microscopy and mercury intrusion,” Journal of the American Ceramic Society, vol. 91, no. 12, p. 4059–4067, 2008.
- [68] L. Froboese, P. Titscher, B. Westphal, W. Haselrieder, and A. Kwade, “Mercury intrusion for ion- and conversion-based battery electrodes - structure and diffusion coefficient determination,” Materials Characterization, vol. 133, p. 102–111, 2017.
- [69] M. Sahimi, Flow and Transport in Porous Media and Fractured Rock: From Classical Methods to Modern Approaches. Weinheim: Wiley, 2<sup>nd</sup> ed., 2011.
- [70] B. Priffing, M. Röding, P. Townsend, M. Neumann, and V. Schmidt, “Large-scale statistical learning for mass transport prediction in porous materials using 90,000 artificially generated microstructures,” Frontiers in Materials, vol. 8, p. 786502, 2021.
- [71] O. Stenzel, O. M. Pecho, L. Holzer, M. Neumann, and V. Schmidt, “Predicting effective conductivities based on geometric microstructure characteristics,” AIChE Journal, vol. 62, no. 5, p. 1834–1843, 2016.
- [72] L. Holzer, D. Wiedenmann, B. Münch, L. Keller, M. Prestat, P. Gasser, I. Robertson, and B. Grobéty, “The influence of constrictivity on the effective transport properties of porous layers in electrolysis and fuel cells,” Journal of Materials Science, vol. 48, p. 2934–2952, 2013.
- [73] M. B. Clennell, “Tortuosity: a guide through the maze,” Geological Society, London, Special Publications, vol. 122, no. 1, p. 299–344, 1997.
- [74] B. Ghanbarian, A. G. Hunt, R. P. Ewing, and M. Sahimi, “Tortuosity in porous media: a critical review,” Soil Science Society of America Journal, vol. 77, no. 5, p. 1461–1477, 2013.

- [75] B. Tjaden, D. J. L. Brett, and P. R. Shearing, “Tortuosity in electrochemical devices: a review of calculation approaches,” International Materials Reviews, vol. 63, no. 2, p. 47–67, 2018.
- [76] D. Jungnickel, Graphs, Networks and Algorithms. Berlin: Springer, 3<sup>rd</sup> ed., 2007.
- [77] M. Neumann, C. Hirsch, J. Staněk, V. Beneš, and V. Schmidt, “Estimation of geodesic tortuosity and constrictivity in stationary random closed sets,” Scandinavian Journal of Statistics, vol. 46, no. 3, p. 848–884, 2019.
- [78] H. Wadell, “Volume, shape, and roundness of quartz particles,” The Journal of Geology, vol. 43, p. 250–280, 1935.

## Supplementary Information

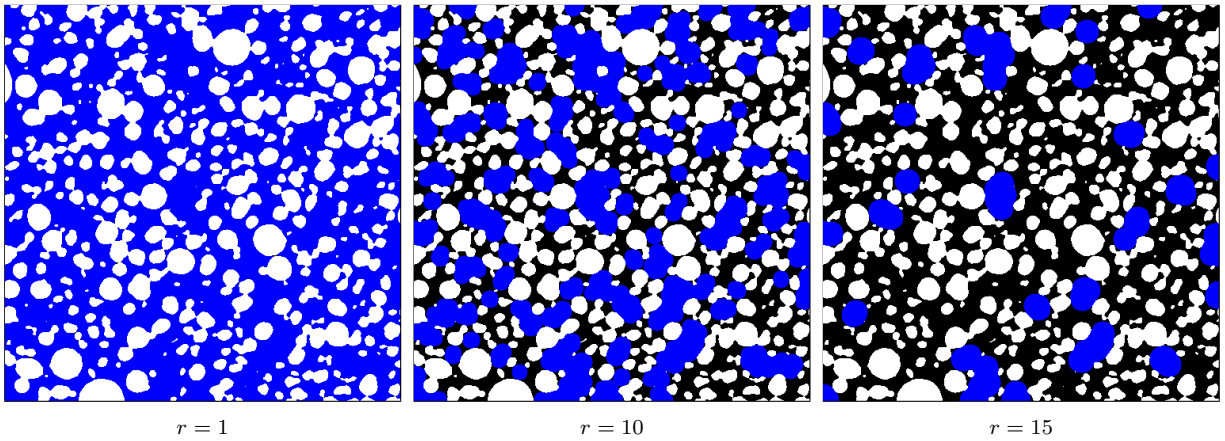


Figure S1: Two-dimensional visualization of the continuous phase size distribution  $\text{CPSD}(r)$  for different radii  $r$  (given in pixels). The example slice is taken from the uncompacted thick sample ( $B_1$ ), where the active material is shown in white. The bap-phase is partitioned into a blue and a black part, where the blue part corresponds to the union of (potentially overlapping) spheres with radius  $r$  that can be placed inside the bap-phase without intersecting the active material. The value  $\text{CPSD}(r)$  is given by the ratio of the area of the blue phase and the area of the bap-phase.

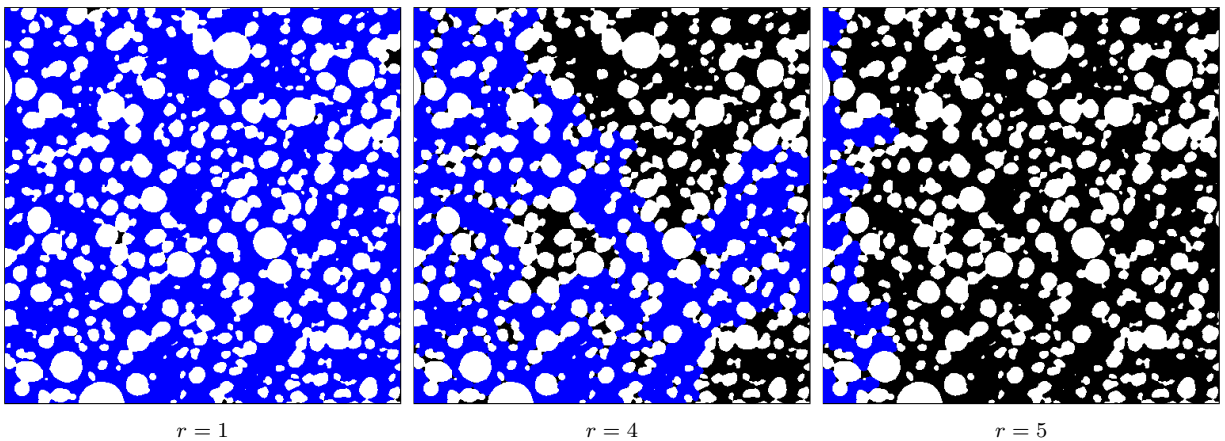


Figure S2: Two-dimensional visualization of the simulated mercury intrusion porosimetry  $\text{MIP}(r)$  for different radii  $r$  (given in pixels). The example slice is taken from the uncompacted thick sample ( $B_1$ ), where the active material is shown in white. The bap-phase is partitioned into a blue and a black part, where the blue part corresponds to the intrusion of the bap-phase with (potentially overlapping) spheres with radius  $r$  from the left. The value  $\text{MIP}(r)$  is given by the ratio of the area of the blue phase and the area of the bap-phase.

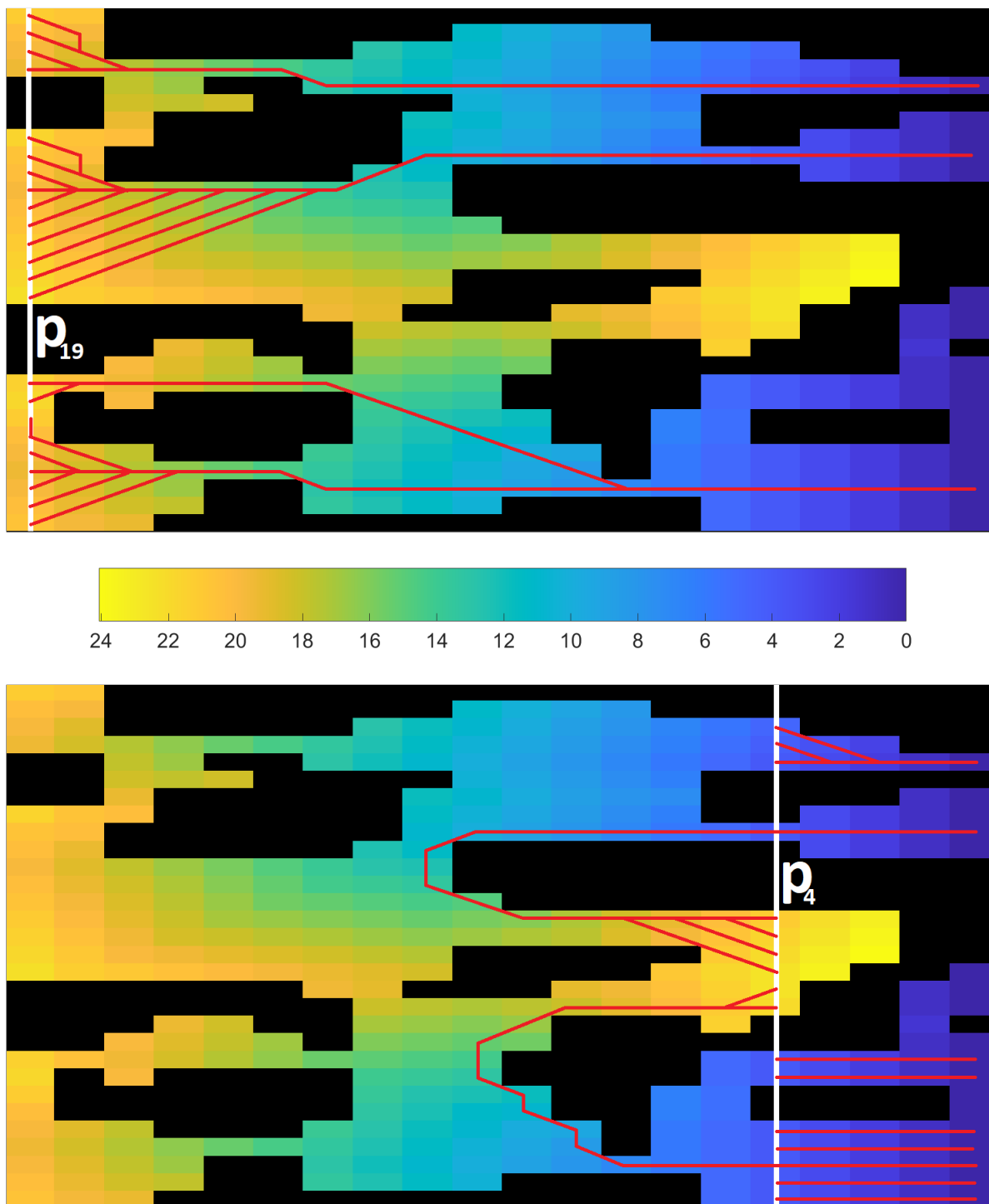


Figure S3: Two-dimensional visualization of the  $p_{19}$  (top) and  $p_4$  (bottom) planes (white) together with the shortest paths starting at considered plane (red). The underlying image is the shortest distance image, where the color of each pixel represents the shortest path length to the right image boundary.